

Particle swarm optimization of a wind farm layout with active control of turbine yaw

Jeonghwan Song¹, Taewan Kim¹, Donghyun You*

*Department of Mechanical Engineering, Pohang University of Science and Technology,
77 Cheongam-Ro, Nam-Gu, Pohang, Gyeongbuk 37673, South Korea*

Abstract

Active yaw control (AYC) of wind turbines has been widely applied to increase the annual energy production (AEP) of a wind farm. AYC efficiency depends on the wind direction and the wind farm layout because an AYC method utilizes wake deflection by yawing wind turbines. Conventional optimization of a wind farm layout assumed that the swept areas of all wind turbines are aligned perpendicular to the wind direction, thereby allowing non-optimal utilization of an AYC method. Higher AEP can be obtained by joint optimization which considers an AYC method in the layout design stage. Joint optimization of the farm layout and AYC has been difficult due to the non-convexity of the problem and the computational inefficiency. In the present study, a particle swarm optimization based method is developed for joint optimization. The layout is optimized with simultaneous consideration for yaw angles for all wind velocities to obtain a globally optimal layout. A number of random initial particles consisting of the layout and yaw angles of wind turbines reduce the initial layout dependency on the optimized layout. To deal with the challenge of large-scale optimization, the adap-

*Corresponding author.

Email address: dhyou@postech.ac.kr (Donghyun You)

¹Authors contributed equally.

tive granularity learning distributed particle swarm optimization algorithm is implemented. The improvement in AEP when using a jointly optimized layout compared to a conventionally optimized layout in a real wind farm is demonstrated using the present method.

Keywords: Wind farm layout optimization, Active yaw control, Particle swarm optimization, Annual energy production

1. Introduction

The annual energy production (AEP) of a wind farm is significantly reduced by wake interactions [1–3]. Once a wind turbine converts wind energy into electrical energy, a wake region with a lower wind speed than its surroundings is created. The power production of a wind turbine in the wake region is lower than that of an upstream wind turbine due to the velocity deficit. Therefore, the way to increase AEP of a wind farm is to reduce the overlap of the wind turbine swept areas and the wake regions as much as possible. For this purpose, two main strategies, optimization of a wind farm layout [4–13] and active wind turbine control [14–22] have been utilized. Layout optimization shifts the positions of wind turbines to separate downstream wind turbines from wake regions. Active wind turbine control changes the blade pitch angle and the rotor tilt and yaw angles to weaken or deflect the wake of a wind turbine. Among current active control options, active yaw control (AYC) is the most promising strategy because of its large wake deflections and the small effect on the structural loads [19–23].

An optimal layout of a wind farm depends on the condition of the wind farm, such as the wind turbine model, the number of turbines, the land size,

and the wind rose. Layout optimization often becomes a highly non-convex and complex problem, therefore meta-heuristic optimization algorithms have been used to solve. The most commonly used algorithms are evolutionary computation algorithms, including genetic algorithms and particle swarm optimization (PSO) algorithms [7, 24–31]. However, as the number of turbines of a layout optimization problem increases, the problem becomes non-convex and leads to non-optimal local minima. To search for a globally optimal solution to a large-scale problem of layout optimization, improved algorithms have been developed [23, 32, 33].

AYC steers the yaw angles of wind turbines to separate downstream wind turbines from wake regions. The efficiency of AYC for a wind farm depends on the wind farm layout and the wind direction. AYC is more efficient for particular wind directions where turbines are more affected by the wake. In the Horns-Rev wind farm, the highest AYC efficiency can be achieved when the wind direction is aligned with turbine rows [19, 23].

The effect of AYC on an optimal layout has recently been studied. The conventional layout optimization problem assumed swept areas of all wind turbines are aligned perpendicular to the wind direction, which is called the greedy control strategy [4–13]. AYC can be optimized after the wind farm layout is optimized, which is defined as sequential optimization. Optimal AYC can generate power more or equal to the greedy strategy [19, 22, 23]. When AYC is considered at the layout design stage, which is defined as joint optimization, the optimized layout can generate power more or equal to the sequentially optimized layout [34]. However, the dimension of the joint optimization problem is significantly increased because the yaw angles of wind

turbines have to be optimized for each wind velocity. Chen *et al.* [34] designed a decomposition-based hybrid method (DBHM) to reduce the computational costs of the joint optimization problem. Starting from the sequentially optimized layout, the optimization problem was decomposed into subproblems that optimized the layout and yaw angles for each wind velocity. The layout of the whole problem was updated based on the alternating direction method of multipliers (ADMM) using optimal solutions to subproblems. This approach successfully lowered the computational cost, but the optimal solution of DBHM highly depends on the initial layout. Also, to converge to a globally optimal solution with high accuracy, ADMM can be very slow [35].

AEP of the optimized wind farm is directly linked to investment gains, therefore finding a globally optimal layout is very important for economic reasons. The yaw angles for each wind velocity can be separately optimized, but the layout cannot be separated for each wind velocity. A decomposition-based method showed the low performance when dealing with partially separable problems [36]. For partially separable and large-scale problems, such as layout optimization, algorithms that deal with the whole problem at once perform better [37–43].

In the present study, a PSO-based layout optimization method with simultaneous consideration of yaw angles for all wind velocities is developed to find a globally optimal layout. Since the present method does not start from one initial layout but uses a number of random initial particles consisting of layouts and yaw angles, the solution of the present method does not depend on one initial layout. Particles are updated towards the layout that simultaneously maximizes AEP for all wind velocities using information of

the optimal particle of each iteration.

In the present work, an adaptive granularity learning distributed particle swarm optimization (AGLDPSO) algorithm is employed, which treats a large-scale problem as a whole to avoid local minima [36]. The present method shows outstanding optimization performance in solving a joint optimization problem. The optimal layout of the present method and that of the previous method in a joint optimization problem are compared. Also, in order for joint optimization to be useful for industrial sites, the joint optimization performance of the following wind farm design conditions is analyzed:

1. Power curve gradients of wind turbines,
2. Number of wind turbines per area,
3. Wind uniformity.

Because a yawed wake is a three-dimensional phenomenon, an in-house code is developed to calculate three-dimensional wind farm power, and the method to solve the joint optimization is developed using the code.

The paper is organized as follows: in Section 2, the theoretical components in the wind farm power calculation and the optimization method are explained in detail. In Section 3, the configurations of the layout optimization problem are defined. The results and discussion of the problems considered are presented in Section 4, followed by concluding remarks in Section 5.

2. Background

2.1. Yawed Gaussian wake model

The velocity of wind passing through each wind turbine needs to be calculated to obtain AEP of a wind farm. The velocity field in a wind farm depends on wake effects. Wake models which can analytically derive the wake velocity are being developed because their lower computational costs benefit layout optimization [44–46]. To optimize AYC, a yawed wake model that considers wake steering by yaw control is needed. Dou *et al.* [23] developed a Gaussian-based yawed wake model which estimates the shape of the wake velocity distribution in the streamwise direction. The model equation can be written as follows:

$$\begin{aligned} \frac{\Delta u}{u_\infty} &= \left(1 - \sqrt{1 - \frac{C_{T*} \cos \gamma}{8\sigma_{\text{yaw}}\sigma_z}} \right) \\ &\times \exp \left[-\frac{1}{2\sigma_{\text{yaw}}^2} \left(\frac{y - Y_{\text{offset},z}}{D \cos \gamma} \right)^2 - \frac{1}{2\sigma_z^2} \left(\frac{z - z_{\text{hub}}}{D} \right)^2 \right], \end{aligned} \quad (1)$$

where

$$\begin{aligned} \delta_* &= 0.607, \zeta = 0.75, k = 0.0125 \\ \delta &= \delta_* C_T, C_{T*} = C_T \cos^2 \gamma, \\ \beta &= (1 + \sqrt{1 - C_{T*} \cos \gamma}) / (2\sqrt{1 - C_{T*} \cos \gamma}), \\ \sigma_{\text{yaw}} &= kx / (D \cos \gamma) + \sqrt{\beta}/5, \\ \sigma_z &= kx/D + \sqrt{\beta}/5, \\ Y_{\text{offset}}/D &= \delta (C_T \sin \gamma)^\zeta \cos^{2\zeta} \gamma \sqrt{x/D} + d_{rt} \sin \gamma / D, \\ Y_{\text{offset},z} &= (Y_{\text{offset}} - d_{rt} \sin \gamma) \exp[-0.5(z - z_{\text{hub}})^2 / (D\sigma_z)^2] + d_{rt}. \end{aligned}$$

D is the diameter of the wind turbine rotor, z_{hub} is the height of the wind turbine hub, d_{rt} is the distance between the rotor center and the hub center,

γ is the yaw angle of the wind turbine, and C_T is the thrust coefficient of the wind turbine when $\gamma = 0$.

The offset of the wake center Y_{offset} increases proportionally with the square root of the streamwise distance x . Deformation of the wake center in the y direction, $Y_{\text{offset},z}$ follows a Gaussian distribution in the z direction. Fig. 1 shows the different wake shapes of the unyawed and the yawed wakes.

2.2. Wake merging model

Wakes by each turbine in the wind farm interfere with each other, therefore a wake merging model is needed. Four merging models are mainly used to represent wake merging phenomena as follows [47–50]:

$$u(x, y, z) = u_\infty(z) - \sum_{i=1}^n (u_\infty(z) - u_i(x, y, z)), \quad (2)$$

$$u(x, y, z) = u_\infty(z) - \sqrt{\sum_{i=1}^n (u_\infty(z) - u_i(x, y, z))^2}, \quad (3)$$

$$u(x, y, z) = u_\infty(z) - \sqrt{\sum_{i=1}^n (\bar{u}_{in,i} - u_i(x, y, z))^2}, \quad (4)$$

$$u(x, y, z) = u_\infty(z) - \sum_{i=1}^n (\bar{u}_{in,i} - u_i(x, y, z)), \quad (5)$$

where $u(x, y, z)$ is the axial velocity field parallel to the direction of the atmospheric wind velocity, calculated with consideration of wake effects. $u_\infty(z)$ represents the wind speed in the atmosphere unaffected by the wind turbines. $u_i(x, y, z)$ means the wake speed of the i -th wind turbine. $\bar{u}_{in,i}$, which is the average wind speed entering the i -th wind turbine can be calculated as follows:

$$\bar{u}_{in,i} = \frac{1}{A_i} \iint_{A_i} u(r, \theta) r dr d\theta. \quad (6)$$

Eqs. (2) and (3) use $u_\infty(z)$ to calculate the wake deficit caused by each wind turbine. This means that the distance between wind turbines is sufficiently far apart so that $\bar{u}_{in,i}$ is equal to $u_\infty(z)$. Eqs. (4) and (5) use $\bar{u}_{in,i}$ to calculate the wake deficit. This merging model is applicable even when the distance between wind turbines is relatively short. Eqs. (3) and (4) calculate the total wake deficit by summing the squares of the wake deficits of turbines. This method is called the energy deficit superposition. On the other hand, Eqs. (2) and (5) calculate the total wake deficit by calculating the linear sum of the wake deficits of turbines. This method is called the velocity deficit superposition. It is shown that the velocity deficit superposition is more accurate than the energy deficit superposition from a large-eddy simulation study [50]. In the present study, Eq. (5) is used because it considers various distances between wind turbines based on the velocity deficit superposition.

2.3. Optimization algorithm

A single-objective constrained optimization problem can be formulated as

$$\min_{\mathbf{X}} f(\mathbf{X}), \quad \mathbf{X} \in \mathbb{R}^{n \times m}, \quad (7)$$

subject to the constraints

$$g_i(\mathbf{X}) \leq 0, \quad i = 1, \dots, k, \quad (8)$$

where $f(\mathbf{X})$ and $g(\mathbf{X})$ are cost and constraint functions for an $n \times m$ real variable matrix \mathbf{X} . When the number of dimensions exceeds 100, traditional evolutionary computation algorithms lose their effectiveness, which is usually known as the ‘‘curse of dimensionality’’ [43]. In this study, the algorithm for

large-scale optimization is used because considering AYC in layout optimization greatly increases the dimension of \mathbf{X} . AGLDPSO can avoid suboptima with a high convergence speed [36].

AGLDPSO is based on PSO [51]. In PSO, each particle j is updated at every step to find the optimal solution. Each particle has a position matrix \mathbf{X} and a velocity matrix \mathbf{V} which have the same dimension as \mathbf{X} . The searching strategy of PSO is described as follows:

$$\mathbf{X}^{t+1} = \mathbf{X}^t + \mathbf{V}^t, \quad (9)$$

where

$$\mathbf{V}^t = \omega \times \mathbf{V}^{t-1} + c_1 \times \mathbf{R}_1^t \odot (\mathbf{X}_{pbest}^t - \mathbf{X}^t) + c_2 \times \mathbf{R}_2^t \odot (\mathbf{X}_{gbest}^t - \mathbf{X}^t).$$

Superscript t notates the present step, the symbol \odot means element-wise product. \mathbf{X}_{pbest} is the historical best position of \mathbf{X} and \mathbf{X}_{gbest} is the best position of \mathbf{X}_{pbest} . Velocities toward \mathbf{X}_{pbest} and \mathbf{X}_{gbest} are added to the current velocity of each particle. ω is the inertia considering the momentum of the previous movement. c_1 and c_2 are coefficients which can regulate the searching speed. \mathbf{R}_1 and \mathbf{R}_2 are random matrices.

Since all particles are updated toward \mathbf{X}_{gbest} every iteration, it easily falls into a local optimum. To improve its performance, AGLDPSO uses a multi-subpopulation distributed model and an adaptive granularity learning strategy. The searching strategy of AGLDPSO is described as follows:

$$\mathbf{X}_w^{t+1} = \mathbf{X}_w^t + \mathbf{V}_w^t, \quad (10)$$

where

$$\mathbf{V}_w^t = \Omega^t \odot \mathbf{V}_w^{t-1} + c_1 \times \mathbf{R}_1^t \odot (\mathbf{X}_{sbest}^t - \mathbf{X}_w^t) + c_2 \times \mathbf{R}_2^t \odot (\mathbf{X}_{gbest}^t - \mathbf{X}_w^t).$$

Subscript w notates the worst particle in each subpopulation, and Ω is random matrix. \mathbf{X}_{sbest} is the best position of each subpopulation and \mathbf{X}_{gbest} is the best position of \mathbf{X}_{sbest} . In Eq. (10), only the worst particle in each subpopulation is updated to search for the global optimal point. More subpopulations lead to more exploration. In each iteration, AGLDPSO divides the particles into subpopulations of the automatically calculated size. For example, when most particles are close to the global worst particle, the size of the subpopulation becomes smaller to increase the number of subpopulations, and the exploration rate increases. On the other hand, fewer subpopulations lead to less exploration. In Fig. 2, because the number of subpopulations in Fig. 2(a) is more than that in Fig. 2(b), the situation in Fig. 2(a) has a tendency to explore rather than exploit. These mechanisms enhance convergence to an optimal point.

3. Problem setup

3.1. AEP calculation

The free stream velocity $u_\infty(z)$ is calculated using an atmospheric boundary layer equation. The power law equation of an atmospheric boundary layer is as follows:

$$u_\infty(z) = U_{ref}(z/z_{ref})^\alpha, \quad (11)$$

where U_{ref} is the measured wind speed at the reference height z_{ref} and α is an exponent determined empirically. In this study, $U_{ref} = 6\text{m/s}$ or 8m/s , and $z_{ref} = 25\text{m}$. α is set to 0.1 for an offshore wind farm [52]. Fig. 3 shows the profile of the atmospheric boundary layer and the wind turbine wake.

Using $u_\infty(z)$ and the wake merging model, $\bar{u}_{in,i}$ of Eq. (6) can be obtained. Because of wake interactions, $\bar{u}_{in,i}$ must be calculated on wind turbines along the wind direction. Fig. 4 explains how to sort wind turbines along the wind direction. The inner product of the wind vector and the position vector of a wind turbine $\mathbf{u}_\infty \cdot \mathbf{x}$ is calculated to sort wind turbines. Numerical integration in Eq. (6) is conducted using the grid of the wind turbine as represented in Fig. 1.

The power coefficient C_P and the thrust coefficient C_T for each wind turbine are functions of $\bar{u}_{in,i}$. They depend on the type of the wind turbine. Fig. 5 shows the power curves, the power coefficients, and the thrust coefficients of the Vestas V80 and the Vestas V112 models [53, 54]. The generated power of the i -th wind turbine is calculated as follows:

$$P = \sum_i \frac{1}{2} \rho C_P(\bar{u}_{in,i}) \bar{u}_{in,i}^3 A_i. \quad (12)$$

In order to calculate AEP of a wind farm, a probability distribution function $p(U_{\infty,j})$ of the annual wind vector is required. Then, AEP can be obtained as follows:

$$AEP = 365 \times 24 \times \sum_j p(U_{\infty,j}) P|_{u_\infty=U_{\infty,j}}, \quad (13)$$

where $U_{\infty,j}$ is the j -th wind vector of $p(U_{\infty,j})$. Units of P and AEP are [W] and [Wh], respectively.

3.2. Optimization configurations

To solve the optimization problem, an appropriate cost function $C(\mathbf{X})$, constraints, and a variable matrix \mathbf{X} have to be defined. For the joint optimization, which consists of AYC and layout optimization, the cost function

is set as the reciprocal of AEP of a wind farm represented as follows:

$$[\mathbf{X}_{pos}^{joint}, \mathbf{X}_{yaw}^{joint}] = \underset{\mathbf{X}}{\operatorname{argmin}} C(\mathbf{X}), \quad \mathbf{X} \subset \mathbb{R}^{n \times (m+2)}, \quad (14)$$

where

$$\mathbf{X} = [\mathbf{X}_{pos}, \mathbf{X}_{yaw}],$$

$$\mathbf{X}_{pos} = \begin{bmatrix} x_1 & y_1 \\ x_2 & y_2 \\ \vdots & \vdots \\ x_n & y_n \end{bmatrix}, \quad \mathbf{X}_{yaw} = \begin{bmatrix} \gamma_{11} & \gamma_{12} & \cdots & \gamma_{1m} \\ \gamma_{21} & \gamma_{22} & \cdots & \gamma_{2m} \\ \vdots & \vdots & \ddots & \vdots \\ \gamma_{n1} & \gamma_{n2} & \cdots & \gamma_{nm} \end{bmatrix},$$

$$C(\mathbf{X}) = \frac{1}{AEP|_{\mathbf{X}}},$$

subject to constraints

$$x_{min} \leq x_i \leq x_{max}, \quad \forall i, \quad (15)$$

$$y_{min} \leq y_i \leq y_{max}, \quad \forall i, \quad (16)$$

$$(x_i - x_j)^2 + (y_i - y_j)^2 > D^2, \quad \forall i, j. \quad (17)$$

The number of turbines in a wind farm is n , and the wind rose consists of m winds. \mathbf{X} consists of positions and yaw angles of n wind turbines. $AEP|_{\mathbf{X}}$ is AEP of a wind farm where the variable matrix is given as \mathbf{X} . Constraints are defined in Eqs. (15)–(17). Wind turbine positions have to be optimized in the wind farm domain $[x_{min}, x_{max}] \times [y_{min}, y_{max}]$, and the distances between each wind turbine have to be more than the wind turbine diameter D . The present joint optimization algorithm finds the optimal layout $[\mathbf{X}_{pos}^{joint}, \mathbf{X}_{yaw}^{joint}]$ where AEP is the maximum using AGLDPSO.

To analyze the joint optimization performance against the conventional layout optimization, the sequential optimization is defined as follows:

$$\mathbf{X}_{pos}^{seq} = \underset{\mathbf{X}_{pos}}{\operatorname{argmin}} C([\mathbf{X}_{pos}, \Theta]), \quad (18)$$

$$\mathbf{X}_{yaw}^{seq} = \underset{\mathbf{X}_{yaw}}{\operatorname{argmin}} C([\mathbf{X}_{pos}^{seq}, \mathbf{X}_{yaw}]). \quad (19)$$

The conventional layout optimization for finding an optimal layout using a greedy yaw control strategy Θ is first performed. Using its optimal layout \mathbf{X}_{pos}^{seq} , the yaw angles of wind turbines according to m wind directions are optimized to maximize AEP.

4. Results and discussions

4.1. Comparison of optimization methods

The result of the present method is compared to that of DBHM using the WF1 case which is shown in Fig. 6(a). The domain of the WF1 case is defined as $[0\text{m}, 1600\text{m}] \times [0\text{m}, 1600\text{m}]$ and the layout of 25 Vestas V80s is optimized. Wind which has the same speed and the same probability blows from eight directions. U_{ref} is 8 m/s, so $\bar{u}_{in,1}$ in Eq. (6) is 8.85 m/s for the Vestas V80. For comparison of results, $AEP|_{\mathbf{X}=[\mathbf{X}_{pos}^{seq}, \Theta]}$, $AEP|_{\mathbf{X}=[\mathbf{X}_{pos}^{seq}, \mathbf{X}_{yaw}^{seq}]}$, $AEP|_{\mathbf{X}=[\mathbf{X}_{pos}^{joint}, \Theta]}$, and $AEP|_{\mathbf{X}=[\mathbf{X}_{pos}^{joint}, \mathbf{X}_{yaw}^{joint}]}$ are defined as S_{Θ} , S_{AYC} , J_{Θ} , and J_{AYC} , respectively. S_{Θ} indicates AEP of conventional layout optimization based on a greedy control strategy, and J_{AYC} is AEP of the joint optimization.

Optimized layouts of the WF1 case using the sequential optimization method and the present method are shown in Fig. 7. In both layouts, wakes

of the upstream wind turbines are deflected by AYC. Downstream wind turbines are located as far from the wake region as possible. The difference in power production between greedy control and AYC is shown in Table 1. Improvements of S_{AYC} , J_{Θ}^{DBHM} , J_{AYC}^{DBHM} , J_{Θ}^{AGLD} , and J_{AYC}^{AGLD} compared to S_{Θ} are shown. Superscripts *DBHM* and *AGLD* represent that the results are optimized using the DBHM and the AGLDPSO algorithms, respectively. S_{Θ} is AEP of the optimized layout using greedy control Θ , so J_{Θ} has to be lower than S_{Θ} . It means that the optimal layout of the joint optimization problem is the solution by AYC, not by greedy control. AEP of AYC is always higher than AEP of greedy control and these improvements are higher for the jointly optimized layout than the sequentially optimized layout. As a result, J_{AYC}^{AGLD} is 3.73% higher than S_{Θ} . Compared to S_{AYC} , J_{AYC}^{AGLD} is 2.42% higher. To maximize the efficiency of AYC, the joint optimization problem must be solved at the design stage of a wind farm layout.

In Table 1, J_{AYC}^{DBHM} is 2.08% higher than S_{Θ} , but it is 1.62% lower than J_{AYC}^{AGLD} . The main differences between the DBHM method and the present method are the initialization of \mathbf{X} and the searching strategy. The DBHM method starts with an optimal layout of the sequential optimization problem and uses the optimal layouts of decomposed subproblems at every optimization step. The solution of the DBHM method depends on the initial layout \mathbf{X}_{pos}^{seq} . On the other hand, The present method searches the globally optimal solution for all wind velocities among particles which start from numerous randomly distributed initial layouts. As a result, $\|\mathbf{X}_{pos}^{joint} - \mathbf{X}_{pos}^{seq}\|_2$ of the DBHM method is found to be 59 m, while that of the present method is 1580 m.

The optimal layout of the joint optimization problem can be very different from that of the sequential optimization problem. The present method searches for a globally optimal layout of joint optimization and does not depend on an initial layout. Therefore, the present method is more accurate for large-scale joint optimization than the DBHM method, which starts from an initial layout. In this study, the remaining case results are obtained using the present method.

4.2. Power curve gradients of wind turbines

Commercial wind turbines have their own characteristics, such as power efficiency and design parameters. These differences affect the optimal layout of the joint optimization problem and the improvement of J_{AYC} compared to S_{AYC} . To investigate the effects of the wind speed and the wind turbine model on joint optimization performance, two modified WF1 cases are considered. For the first case, U_{ref} is changed from 8 m/s to 6 m/s, and for the second case, the wind turbine model is changed from the Vestas V80 to the Vestas V112. The results are shown in Table 2.

The improvement of J_{AYC} compared to S_{AYC} with U_{ref} of 6 m/s is 1.56% lower than that of the WF1 case. On the other hand, the improvement of J_{AYC} compared to S_{AYC} of the Vestas V112 case is 1.90% higher than that of the WF1 case. In Fig. 5(c), when the wind speed is less than 9 m/s, the C_T of both wind turbines are almost the same. This means the wake characteristics normalized by U_{ref} are also similar. The main reason for the difference in the improvements of J_{AYC} compared to S_{AYC} can be explained using the magnitude of the power gradient. In Fig. 8(a), normalized power curves $\mathcal{P} = P/P_{rated}$ of the Vestas V80 and the Vestas V112 are shown.

The denominator is selected as the rated power of each wind turbine for generalization. Fig. 8(b) shows the gradient of the normalized power curves \mathcal{P} .

In Table 3, $\bar{\mathcal{P}}_{up}$ and $\bar{\mathcal{P}}_{down}$ are shown. Subscript *up* means upstream wind turbines where the generated power decreased by AYC and subscript *down* means downstream wind turbines where the generated power is increased by AYC. $\bar{\mathcal{P}}_{up}$ and $\bar{\mathcal{P}}_{down}$ represent normalized power averaged by the number of upstream and downstream wind turbines, respectively. $\bar{\mathcal{P}}_{up}$ is higher than $\bar{\mathcal{P}}_{down}$ because winds through the upstream wind turbines are not much affected by the wake. As shown in Fig. 8, the power gradients of both wind turbines monotonically increase until 9 m/s. Therefore, upstream wind turbines are in a higher power gradient region than downstream wind turbines. In all cases, $(\frac{\Delta\bar{\mathcal{P}}}{\Delta u_{in}})_{up}$ is higher than $(\frac{\Delta\bar{\mathcal{P}}}{\Delta u_{in}})_{down}$. However, $|\Delta\bar{\mathcal{P}}_{up}|$ is lower than $|\Delta\bar{\mathcal{P}}_{down}|$ because the velocity decrease of an upstream wind turbine which is proportional to $\cos\gamma$ is much smaller than the velocity increase of a downstream wind turbine. Deflection of the wake increases as it flows downstream. The difference between $|\Delta\bar{\mathcal{P}}_{up}|$ and $|\Delta\bar{\mathcal{P}}_{down}|$, which is the net power improvement by AYC, is higher when the wind turbines are in a high power gradient region. For the Vestas V80, the power gradient of $U_{ref} = 8$ m/s case is higher than that of $U_{ref} = 6$ m/s case. Similarly, the power gradient of the Vestas V112 is higher than that of the Vestas V80. As the efficiency of AYC becomes higher, the efficiency of the joint optimization increases.

4.3. Number of turbines per area

The grid interval of the checkerboard layout of the WF1 case is $5D$ as shown in Fig. 6(a). To investigate the effect of the wind farm area on joint

optimization efficiency, the grid interval of the WF2 case is increased to $6D$, and the number of wind turbines is maintained, as shown in Fig. 6(b). This leads the average distance between wind turbines of an optimized layout to increase. Table 4 shows that AEP of the WF2 case is improved compared to AEP of the WF1 case because the velocity deficit due to the wake is inversely proportional to the distance. The WF2 case is less affected by the wake than the WF1 case. On the other hand, power improvement using AYC instead of the greedy strategy in the WF2 case is found to be lower than that observed in the WF1 case. As the wake velocity deficit becomes smaller, the maximum power gain of the downstream turbine by AYC decreases, so the AYC efficiency reduces. As a result, improvement of J_{AYC} compared to S_{AYC} of the WF2 case is 1.97% smaller than that of the WF1 case.

In the WF3 case, the grid interval is the same as in the WF2 case as shown in Fig. 6c, so the wake deficit of wind turbines is similar. In the WF3 case, the number of wind turbines is increased to 36. Table 4 shows power improvement using AYC instead of the greedy strategy in the WF3 case is lower than that observed in the WF2 case. As the number of wind turbines increases, deflected wake regions due to AYC are more likely to overlap with other downstream wind turbines. Therefore, improving the total AEP of the wind farm using AYC is much more difficult. On the other hand, improvement in J_{AYC} compared to S_{AYC} of the WF3 case is 0.45% higher than that of the WF2 case. This is because the effect of distributing the wake zone by simply changing the positions of wind turbines is lowered for a large number of wind turbines. The possibility of the downstream wind turbines being in the wake zone, which is parallel to the wind direction, increases. In

the sequential optimization problem, the layout is not optimized considering wake deflection, so it cannot efficiently use AYC as in the joint optimization problem.

4.4. Wind uniformity

To investigate the effect of wind uniformity on the joint optimization efficiency, uneven winds are supposed in the WF4 case, as shown in Fig. 6(d). The wind from the west has a magnitude of 11 m/s and the probability of the wind is 20% and the winds from the northwest and the southwest have a magnitude of 9 m/s and the probability of 15% in each direction. The winds from the other directions have a magnitude of 8 m/s and the probability of 10%. In Table 4, improvement of J_{AYC} compared to S_{AYC} of the WF4 case is 1.44% lower than that in the WF1 case. This can be explained by analyzing the efficiency of the optimal layout of the joint optimization problem for each wind direction. Table 5 shows the difference in the mean AEP of (1) the west, (2) the northwest and the southwest, and (3) the other directions. Unlike directions (2) and (3), the wind energy of direction (1) is significantly large. This means that especially optimizing the wind farm layout for the wind from the west is advantageous in improving the total AEP of the wind farm. Then, the degrees of freedom of the layout in the other directions is lowered, and the wake effect in those directions is increased. In Table 5, J_{AYC} of direction (1) accounts for 59.2% of the sum of mean J_{AYC} of directions (1), (2), and (3). The improvements of AYC compared to the greedy strategy increases in the order of directions (1), (2), and (3) because AEP loss caused by the wake increases in that order. Because improvement of J_{AYC} compared to S_{AYC} of direction (1) in the WF4 case is much less than that in the WF1

case, the efficiency of the joint optimization of the WF4 case is lower than that in the WF1 case.

5. Concluding remarks

A particle swarm optimization based optimization method for a wind farm layout with consideration of active yaw control has been developed, and its effectiveness has been analyzed. In the present method, a wind farm layout is optimized with simultaneous consideration of yaw angles for all wind velocities to find a globally optimal layout of the joint optimization problem. An in-house code has been developed to calculate the power production of a wind farm using three-dimensional wake and wake merging models, while the annual energy production of the wind farm has been optimized using locations and yaw angles of wind turbines as control variables. The present method uses an adaptive granularity learning distributed particle swarm optimization algorithm and shows outstanding capability in large-scale joint optimization problems. In the WF1 case, which has been used to optimize the layout of 25 Vestas V80 wind turbines considering a uniform wind velocity of 8 m/s in a square-shaped wind farm with a side length of 1600 m, the annual energy production of the present method has been 1.62% higher than that of the previous method.

Efficiencies of joint optimization problems of the following conditions have been analyzed. Firstly, the effect of the power curve gradient on optimization has been analyzed. Two modified WF1 cases which have different free stream velocities and the wind turbine model have been optimized. The larger the power curve gradient, the higher the efficiency of active yaw control. When

the Vestas V112 was used for the WF1 case, J_{AYC} has been increased by 4.32% than S_{AYC} . Secondly, the WF2 case and the WF3 case, which have different wind farm areas and the number of wind turbines, have been optimized. It has been shown that the efficiency of joint optimization increases as the size of the wind farm decreases and as the number of wind turbines increases. Finally, the effect of the uniformity of winds has been analyzed. In the WF4 case, which supposed uneven winds, because the layout has been optimized to the direction where the wind energy is rich, the efficiency of the joint optimization has been lower than in the WF1 case.

The annual energy production of the jointly optimized layout using the proposed method has been higher than that of the sequentially optimized layout. When designing a jointly optimized layout, the annual energy production with simultaneous consideration of all wind velocities has been higher than that of separately considering wind velocities. The presented method can adopt massive variables and constraints of layout optimization problems and can be widely applied to improve actual wind farm design.

Acknowledgements

The work was supported by the National Research Foundation of Korea (NRF) under the Grant Number NRF-2021R1A2C2092146 and the Korea Electric Power Corporation (KEPCO) under the Grant No. R20XO02-21.

References

- [1] R. J. Barthelmie, K. Hansen, S. T. Frandsen, O. Rathmann, J. G. Schepers, W. Schlez, J. Phillips, K. Rados, A. Zervos, E. S. Politis, P. K. Chaviaropoulos, Modelling and measuring flow and wind turbine wakes in large wind farms offshore, *Wind Energy* 12 (5) (2009) 431–444.
- [2] J. Cleve, M. Greiner, P. Enevoldsen, B. Birkemose, L. Jensen, Model-based analysis of wake-flow data in the Nysted offshore wind farm, *Wind Energy* 12 (2) (2009) 125–135.
- [3] R. J. Barthelmie, L. Jensen, Evaluation of wind farm efficiency and wind turbine wakes at the Nysted offshore wind farm, *Wind Energy* 13 (6) (2010) 573–586.
- [4] L. Parada, C. Herrera, P. Flores, V. Parada, Wind farm layout optimization using a Gaussian-based wake model, *Renewable Energy* 107 (2017) 531–541.
- [5] W. Li, E. Özcan, R. John, Multi-objective evolutionary algorithms and hyper-heuristics for wind farm layout optimisation, *Renewable Energy* 105 (2017) 473–482.
- [6] S. A. MirHassani, A. Yarahmadi, Wind farm layout optimization under uncertainty, *Renewable Energy* 107 (2017) 288–297.
- [7] C. Wu, X. Yang, Y. Zhu, On the design of potential turbine positions for physics-informed optimization of wind farm layout, *Renewable Energy* 164 (2021) 1108–1120.

- [8] T. Zilong, D. X. Wei, Layout optimization of offshore wind farm considering spatially inhomogeneous wave loads, *Applied Energy* 306 (2022) 117947.
- [9] S. R. Reddy, Wind farm layout optimization (WindFLO): An advanced framework for fast wind farm analysis and optimization, *Applied Energy* 269 (2020) 115090.
- [10] E. G. Antonini, D. A. Romero, C. H. Amon, Continuous adjoint formulation for wind farm layout optimization: A 2D implementation, *Applied Energy* 228 (2018) 2333–2345.
- [11] J. Y. Kuo, D. A. Romero, J. C. Beck, C. H. Amon, Wind farm layout optimization on complex terrains – integrating a CFD wake model with mixed-integer programming, *Applied Energy* 178 (2016) 404–414.
- [12] K. Yang, G. Kwak, K. Cho, J. Huh, Wind farm layout optimization for wake effect uniformity, *Energy* 183 (2019) 983–995.
- [13] H. Long, P. Li, W. Gu, A data-driven evolutionary algorithm for wind farm layout optimization, *Energy* 208 (2020) 118310.
- [14] A. M. Boulamatsis, T. K. Barlas, H. Stapountzis, Active control of wind turbines through varying blade tip sweep, *Renewable Energy* 131 (2019) 25–36.
- [15] A. Cooperman, M. Martinez, Load monitoring for active control of wind turbines, *Renewable and Sustainable Energy Reviews* 41 (2015) 189–201.

- [16] E. J. N. Menezes, A. M. Araújo, N. S. B. Da Silva, A review on wind turbine control and its associated methods, *Journal of Cleaner Production* 174 (2018) 945–953.
- [17] X. Tang, M. Yin, C. Shen, Y. Xu, Z. Y. Dong, Y. Zou, Active power control of wind turbine generators via coordinated rotor speed and pitch angle regulation, *IEEE Transactions on Sustainable Energy* 10 (2) (2018) 822–832.
- [18] M. Lin, F. Porté-Agel, Power maximization and fatigue-load mitigation in a wind-turbine array by active yaw control: an LES study, in: *Journal of Physics: Conference Series*, Vol. 1618, IOP Publishing, 2020, p. 042036.
- [19] H. Zong, F. Porté-Agel, Experimental investigation and analytical modelling of active yaw control for wind farm power optimization, *Renewable Energy* 170 (2021) 1228–1244.
- [20] D. Song, Z. Li, L. Wang, F. Jin, C. Huang, E. Xia, R. M. Rizk-Allah, J. Yang, M. Su, Y. H. Joo, Energy capture efficiency enhancement of wind turbines via stochastic model predictive yaw control based on intelligent scenarios generation, *Applied Energy* 312 (2022) 118773.
- [21] D. Song, X. Fan, J. Yang, A. Liu, S. Chen, Y. H. Joo, Power extraction efficiency optimization of horizontal-axis wind turbines through optimizing control parameters of yaw control systems using an intelligent method, *Applied Energy* 224 (2018) 267–279.

- [22] H. Ma, M. Ge, G. Wu, B. Du, Y. Liu, Formulas of the optimized yaw angles for cooperative control of wind farms with aligned turbines to maximize the power production, *Applied Energy* 303 (2021) 117691.
- [23] B. Dou, T. Qu, L. Lei, P. Zeng, Optimization of wind turbine yaw angles in a wind farm using a three-dimensional yawed wake model, *Energy* 209 (2020) 118415.
- [24] Y. Wu, S. Zhang, R. Wang, Y. Wang, X. Feng, A design methodology for wind farm layout considering cable routing and economic benefit based on genetic algorithm and GeoSteiner, *Renewable Energy* 146 (2020) 687–698.
- [25] X. Ju, F. Liu, Wind farm layout optimization using self-informed genetic algorithm with information guided exploitation, *Applied Energy* 248 (2019) 429–445.
- [26] S. M. Masoudi, M. Baneshi, Layout optimization of a wind farm considering grids of various resolutions, wake effect, and realistic wind speed and wind direction data: A techno-economic assessment, *Energy* (2022) 123188.
- [27] R. Brogna, J. Feng, J. N. Sørensen, W. Z. Shen, F. Porté-Agel, A new wake model and comparison of eight algorithms for layout optimization of wind farms in complex terrain, *Applied Energy* 259 (2020) 114189.
- [28] N. Kirchner-Bossi, F. Porté-Agel, Realistic wind farm layout optimization through genetic algorithms using a Gaussian wake model, *Energies* 11 (12) (2018) 3268.

- [29] S. Tao, Q. Xu, A. Feijóo, G. Zheng, J. Zhou, Wind farm layout optimization with a three-dimensional Gaussian wake model, *Renewable Energy* 159 (2020) 553–569.
- [30] S. Chowdhury, J. Zhang, A. Messac, L. Castillo, Unrestricted wind farm layout optimization (UWFLO): Investigating key factors influencing the maximum power generation, *Renewable Energy* 38 (1) (2012) 16–30.
- [31] P. Hou, W. Hu, M. Soltani, C. Chen, Z. Chen, Combined optimization for offshore wind turbine micro siting, *Applied Energy* 189 (2017) 271–282.
- [32] J. Patel, V. Savsani, V. Patel, R. Patel, Layout optimization of a wind farm to maximize the power output using enhanced teaching learning based optimization technique, *Journal of Cleaner Production* 158 (2017) 81–94.
- [33] S. Pookpant, W. Ongsakul, Design of optimal wind farm configuration using a binary particle swarm optimization at Huasai district, Southern Thailand, *Energy Conversion and Management* 108 (2016) 160–180.
- [34] K. Chen, J. Lin, Y. Qiu, F. Liu, Y. Song, Joint optimization of wind farm layout considering optimal control, *Renewable Energy* 182 (2022) 787–796.
- [35] S. Boyd, N. Parikh, E. Chu, B. Peleato, J. Eckstein, et al., Distributed optimization and statistical learning via the alternating direction method of multipliers, *Foundations and Trends in Machine Learning* 3 (1) (2011) 1–122.

- [36] Z.-J. Wang, Z.-H. Zhan, S. Kwong, H. Jin, J. Zhang, Adaptive granularity learning distributed particle swarm optimization for large-scale optimization, *IEEE Transactions on Cybernetics* 51 (3) (2020) 1175–1188.
- [37] R. Cheng, Y. Jin, A social learning particle swarm optimization algorithm for scalable optimization, *Information Sciences* 291 (2015) 43–60.
- [38] R. Cheng, Y. Jin, A competitive swarm optimizer for large scale optimization, *IEEE Transactions on Cybernetics* 45 (2) (2014) 191–204.
- [39] K. C. Tan, Y. Yang, C. K. Goh, A distributed cooperative coevolutionary algorithm for multiobjective optimization, *IEEE Transactions on Evolutionary Computation* 10 (5) (2006) 527–549.
- [40] X.-F. Liu, Z.-H. Zhan, Y. Gao, J. Zhang, S. Kwong, J. Zhang, Coevolutionary particle swarm optimization with bottleneck objective learning strategy for many-objective optimization, *IEEE Transactions on Evolutionary Computation* 23 (4) (2018) 587–602.
- [41] Z.-H. Zhan, X.-F. Liu, H. Zhang, Z. Yu, J. Weng, Y. Li, T. Gu, J. Zhang, Cloudde: A heterogeneous differential evolution algorithm and its distributed cloud version, *IEEE Transactions on Parallel and Distributed Systems* 28 (3) (2016) 704–716.
- [42] Z.-J. Wang, Z.-H. Zhan, W.-J. Yu, Y. Lin, J. Zhang, T.-L. Gu, J. Zhang, Dynamic group learning distributed particle swarm optimization for large-scale optimization and its application in cloud workflow scheduling, *IEEE Transactions on Cybernetics* 50 (6) (2019) 2715–2729.

- [43] H. Wang, M. Liang, C. Sun, G. Zhang, L. Xie, Multiple-strategy learning particle swarm optimization for large-scale optimization problems, *Complex & Intelligent Systems* 7 (1) (2021) 1–16.
- [44] N. O. Jensen, *A note on wind generator interaction*, Vol. 2411, Citeseer, 1983.
- [45] S. Frandsen, R. Barthelmie, S. Pryor, O. Rathmann, S. Larsen, J. Højstrup, M. Thøgersen, Analytical modelling of wind speed deficit in large offshore wind farms, *Wind Energy* 9 (1-2) (2006) 39–53.
- [46] M. Bastankhah, F. Porté-Agel, A new analytical model for wind-turbine wakes, *Renewable Energy* 70 (2014) 116–123.
- [47] P. Lissaman, Energy effectiveness of arbitrary arrays of wind turbines, *Journal of Energy* 3 (6) (1979) 323–328.
- [48] I. Katic, J. Højstrup, N. O. Jensen, A simple model for cluster efficiency, in: *European Wind Energy Association Conference and Exhibition*, Vol. 1, A. Raguzzi Rome, Italy, 1986, pp. 407–410.
- [49] S. Voutsinas, K. Rados, A. Zervos, On the analysis of wake effects in wind parks, *Wind Engineering* 14 (1990) 204–219.
- [50] A. Niayifar, F. Porté-Agel, Analytical modeling of wind farms: A new approach for power prediction, *Energies* 9 (9) (2016) 741.
- [51] R. Eberhart, J. Kennedy, Particle swarm optimization, in: *Proceedings of the IEEE International Conference on Neural Networks*, Vol. 4, Citeseer, 1995, pp. 1942–1948.

- [52] Z. Wang, W. Tian, H. Hu, A comparative study on the aeromechanic performances of upwind and downwind horizontal-axis wind turbines, *Energy Conversion and Management* 163 (2018) 100–110.
- [53] Y.-T. Wu, F. Porté-Agel, Atmospheric turbulence effects on wind-turbine wakes: An LES study, *Energies* 5 (12) (2012) 5340–5362.
- [54] I. Amin, M. E. Ali, S. Bayoumi, A. Balah, S. Oterkus, H. Shawky, E. Oterkus, Numerical hydrodynamics-based design of an offshore platform to support a desalination plant and a wind turbine in Egypt, *Ocean Engineering* 229 (2021) 108598.

List of Tables

- 1 Results of the WF1 case optimizing the layout of 25 Vestas V80 wind turbines considering uniform wind with a velocity of 8 m/s in a square-shaped wind farm with a side length of 1600 m. Configurations of the WF1 are shown in Fig. 6(a). S represents the annual energy production (AEP) of the sequentially optimized result, and J represents AEP of the jointly optimized result. Subscript Θ means turbines are aligned perpendicular to the wind direction. Subscript AYC is the active yaw control (AYC) method where the yaw angles of turbines are optimized to maximize AEP of the wind farm. Superscripts $DBHM$ and $AGLD$ represent that the results are optimized using the decomposition-based hybrid method (DBHM) and the adaptive granularity learning distributed particle swarm optimization (AGLDPSO) algorithms, respectively. 32
- 2 Results of the modified WF1 cases. Both cases optimize the layout of 25 wind turbines in a square-shaped wind farm with a side length of 1600 m. U_{ref} of the case (a) is 6m/s and turbines of the case (a) are Vestas V80. U_{ref} of the case (b) is 8m/s and the turbines of the case (b) are Vestas V112. 33

- 3 Results of J_{AYC} of the WF1 case and of the modified WF1 cases, which have different U_{ref} and the wind turbine model, respectively. \mathcal{P} is the power of a wind turbine normalized by its rated power. Subscript *up* means upstream wind turbines where the generated power decreases due to active yaw control (AYC) and subscript *down* means downstream wind turbines where the generated power increases due to AYC. $\bar{\mathcal{P}}_{up}$ and $\bar{\mathcal{P}}_{down}$ are normalized power averaged by the number of upstream and downstream wind turbines, respectively. Δ means the amount of value changed by AYC. $(\frac{\Delta \mathcal{P}}{\Delta u_{in}})$ represents the averaged derivative of power. 34
- 4 Results of the WF2, WF3, and WF4 cases. For the WF2 case, the layout of 25 Vestas V80 wind turbines is optimized by considering a uniform wind of 8 m/s in a square-shaped wind farm with a side length of 1920 m. For the WF3 case, the layout of 36 Vestas V80 wind turbines is optimized by considering a uniform wind of 8 m/s in a square-shaped wind farm with a side length of 2400 m. For the WF4 case, the layout of 25 Vestas V80 wind turbines is optimized by considering uneven winds in a square-shaped wind farm with a side length of 1600 m. The configurations of the WF2, WF3, and WF4 are shown in Fig. 6(b), Fig. 6(c), and Fig. 6(d), respectively. 35

5 AEP of the WF4 case is divided by directions as follows: (1) AEP when the wind direction is west, (2) mean AEP when the wind directions are northwest and southwest, and (3) mean AEP when the wind comes from the other directions. 36

	S_{Θ}	S_{AYC}	J_{Θ}^{DBHM}	J_{AYC}^{DBHM}	J_{Θ}^{AGLD}	J_{AYC}^{AGLD}
AEP (GWh)	168.46	170.61	167.19	171.96	167.98	174.74
Improvement (%)	-	1.28	-0.75	2.08	-0.29	3.73

Table 1: Results of the WF1 case optimizing the layout of 25 Vestas V80 wind turbines considering uniform wind with a velocity of 8 m/s in a square-shaped wind farm with a side length of 1600 m. Configurations of the WF1 are shown in Fig. 6(a). S represents the annual energy production (AEP) of the sequentially optimized result, and J represents AEP of the jointly optimized result. Subscript Θ means turbines are aligned perpendicular to the wind direction. Subscript AYC is the active yaw control (AYC) method where the yaw angles of turbines are optimized to maximize AEP of the wind farm. Superscripts $DBHM$ and $AGLD$ represent that the results are optimized using the decomposition-based hybrid method (DBHM) and the adaptive granularity learning distributed particle swarm optimization (AGLDPSO) algorithms, respectively.

Modified Variables		S_{Θ}	S_{AYC}	J_{Θ}	J_{AYC}
(a)	$U_{ref} = 6\text{m/s}$				
	AEP (GWh)	69.35	70.62	68.46	71.23
	Improvement (%)	-	1.83	-1.29	2.70
(b)	Vestas V112				
	AEP (GWh)	323.20	333.72	321.04	348.14
	Improvement (%)	-	3.26	-0.67	7.72

Table 2: Results of the modified WF1 cases. Both cases optimize the layout of 25 wind turbines in a square-shaped wind farm with a side length of 1600 m. U_{ref} of the case (a) is 6m/s and turbines of the case (a) are Vestas V80. U_{ref} of the case (b) is 8m/s and the turbines of the case (b) are Vestas V112.

	$\bar{\mathcal{P}}_{up}$	$\Delta\bar{\mathcal{P}}_{up}$	$(\frac{\Delta\bar{\mathcal{P}}}{\Delta u_{in}})_{up}$	$\bar{\mathcal{P}}_{down}$	$\Delta\bar{\mathcal{P}}_{down}$	$(\frac{\Delta\bar{\mathcal{P}}}{\Delta u_{in}})_{down}$
WF1	0.438	-0.020	0.152	0.330	0.055	0.135
$U_{ref} = 6m/s$	0.178	-0.009	0.086	0.134	0.022	0.077
Vestas V112	0.615	-0.059	0.192	0.378	0.133	0.167

Table 3: Results of J_{AYC} of the WF1 case and of the modified WF1 cases, which have different U_{ref} and the wind turbine model, respectively. \mathcal{P} is the power of a wind turbine normalized by its rated power. Subscript *up* means upstream wind turbines where the generated power decreases due to active yaw control (AYC) and subscript *down* means downstream wind turbines where the generated power increases due to AYC. $\bar{\mathcal{P}}_{up}$ and $\bar{\mathcal{P}}_{down}$ are normalized power averaged by the number of upstream and downstream wind turbines, respectively. Δ means the amount of value changed by AYC. $(\frac{\Delta\bar{\mathcal{P}}}{\Delta u_{in}})$ represents the averaged derivative of power.

		S_{Θ}	S_{AYC}	J_{Θ}	J_{AYC}
WF2	AEP (GWh)	180.44	182.53	178.15	183.35
	Improvement (%)	-	1.16	-1.27	1.61
WF3	AEP (GWh)	249.79	251.93	248.97	254.21
	Improvement (%)	-	0.86	-0.33	1.77
WF4	AEP (GWh)	233.96	236.48	232.06	238.80
	Improvement (%)	-	1.08	-0.81	2.07

Table 4: Results of the WF2, WF3, and WF4 cases. For the WF2 case, the layout of 25 Vestas V80 wind turbines is optimized by considering a uniform wind of 8 m/s in a square-shaped wind farm with a side length of 1920 m. For the WF3 case, the layout of 36 Vestas V80 wind turbines is optimized by considering a uniform wind of 8 m/s in a square-shaped wind farm with a side length of 2400 m. For the WF4 case, the layout of 25 Vestas V80 wind turbines is optimized by considering uneven winds in a square-shaped wind farm with a side length of 1600 m. The configurations of the WF2, WF3, and WF4 are shown in Fig. 6(b), Fig. 6(c), and Fig. 6(d), respectively.

Wind		S_{Θ}	S_{AYC}	J_{Θ}	J_{AYC}	$J_{AYC}/(\sum J_{AYC})$
(1)	AEP (GWh)	77.87	78.09	76.73	78.41	59.2%
	Improvement (%)	-	0.29	-1.46	0.70	
(2)	AEP (GWh)	36.26	36.70	35.62	36.76	27.7%
	Improvement (%)	-	1.21	-1.77	1.38	
(3)	AEP (GWh)	16.71	17.00	16.82	17.37	13.1%
	Improvement (%)	-	1.71	0.62	3.95	

Table 5: AEP of the WF4 case is divided by directions as follows: (1) AEP when the wind direction is west, (2) mean AEP when the wind directions are northwest and southwest, and (3) mean AEP when the wind comes from the other directions.

List of Figures

1	(a) Unyawed and (b) yawed wake shapes.	39
2	Subpopulations of multi-swarm particle swarm optimization for different subpopulation sizes. (a) Small size and (b) large size.	40
3	(a) The atmospheric boundary layer profile and (b) the wake velocity profile.	41
4	Schematic illustration of the method sorting wind turbines along the wind direction.	42
5	(a) Power curves, (b) power coefficients, and (c) thrust coefficients of the Vestas V80 (—) and the Vestas V112 (—), respectively.	43

6	<p>Four different optimization cases. (a) Optimization of a layout of 25 Vestas V80 wind turbines considering a uniform wind of 8 m/s in a square-shaped wind farm with a side length of 1600 m. The side length is $4 \times 5D$ where D is the wind turbine diameter (80 m). (b) Optimization of a layout of 25 Vestas V80 wind turbines considering a uniform wind of 8 m/s in a square-shaped wind farm with a side length of 1920 m. The side length is $4 \times 6D$. (c) Optimization of a layout of 36 Vestas V80 wind turbines considering a uniform wind of 8 m/s in a square-shaped wind farm with a side length of 2400 m. The side length is $5 \times 6D$. (d) Optimization of a layout of 25 Vestas V80 wind turbines considering uneven winds in a square-shaped wind farm with a side length of 1600 m. The side length is $4 \times 5D$.</p>	44
7	<p>Contours of wakes of sequentially optimized layouts for the wind from (a) the west, (b) the southwest, and (c) the south. Contours of wakes of jointly optimized layouts for the wind from (a) the west, (b) the southwest, and (c) the south. The color bar corresponds the magnitude of the wake deficit. . . .</p>	45
8	<p>(a) Power curves of wind turbines normalized by the rated power and (b) derivatives of the power curve with respect to wind speed. Wind turbines are the Vestas V80 (—) and the Vestas V112 (—).</p>	46

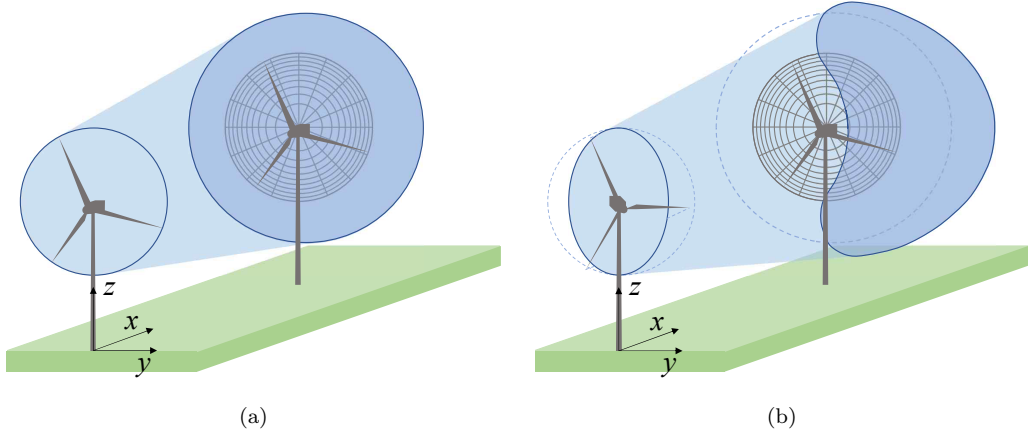


Figure 1: (a) Unyawed and (b) yawed wake shapes.

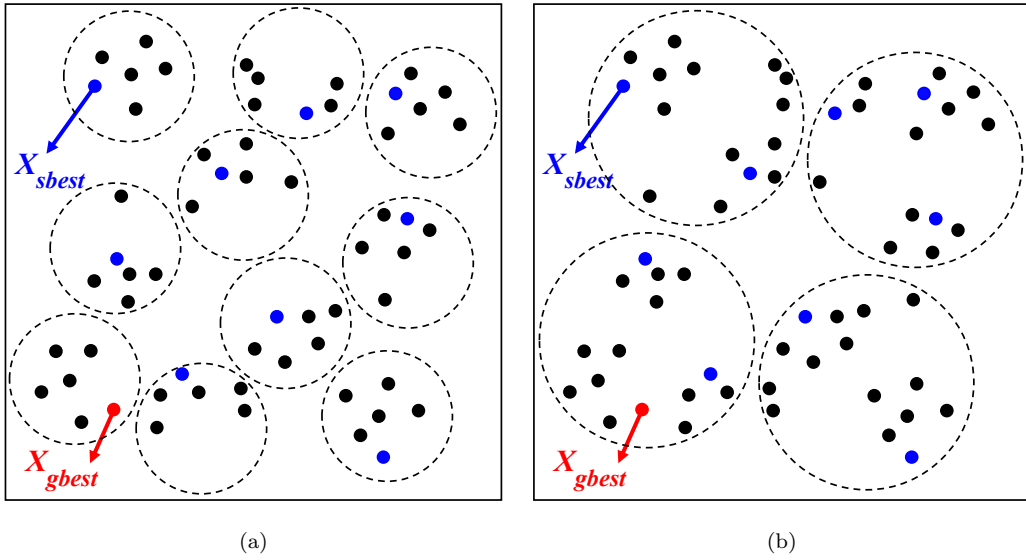


Figure 2: Subpopulations of multi-swarm particle swarm optimization for different subpopulation sizes. (a) Small size and (b) large size.

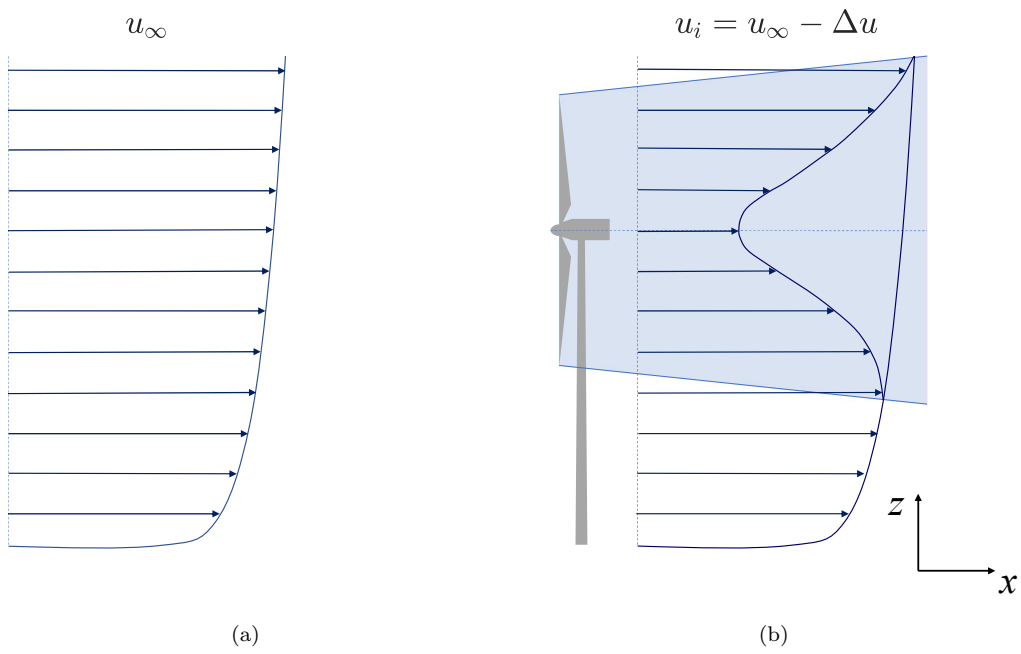


Figure 3: (a) The atmospheric boundary layer profile and (b) the wake velocity profile.

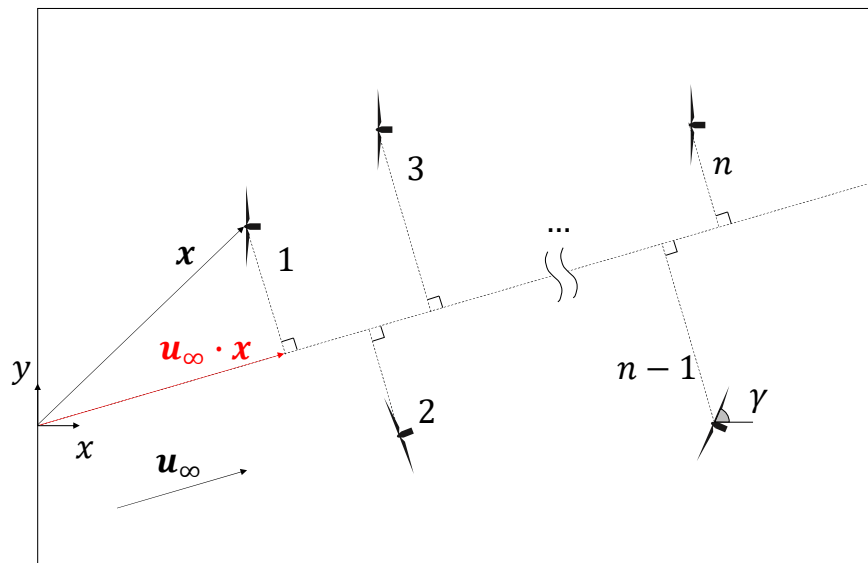


Figure 4: Schematic illustration of the method sorting wind turbines along the wind direction.

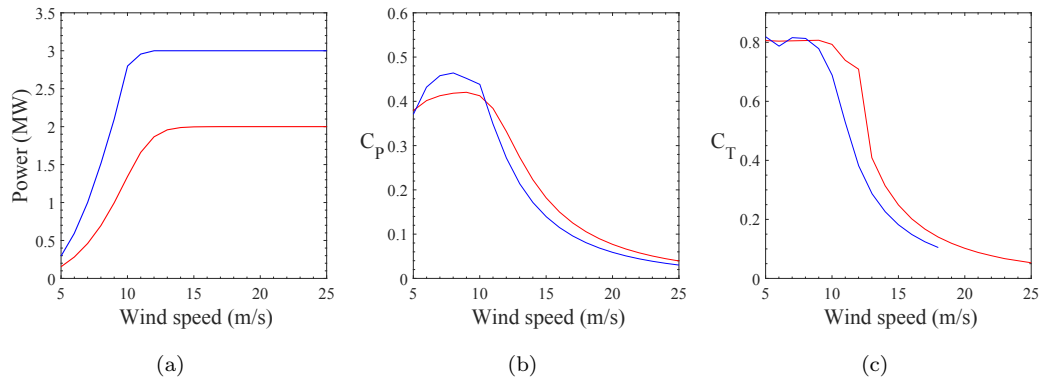


Figure 5: (a) Power curves, (b) power coefficients, and (c) thrust coefficients of the Vestas V80 (—) and the Vestas V112 (—), respectively.

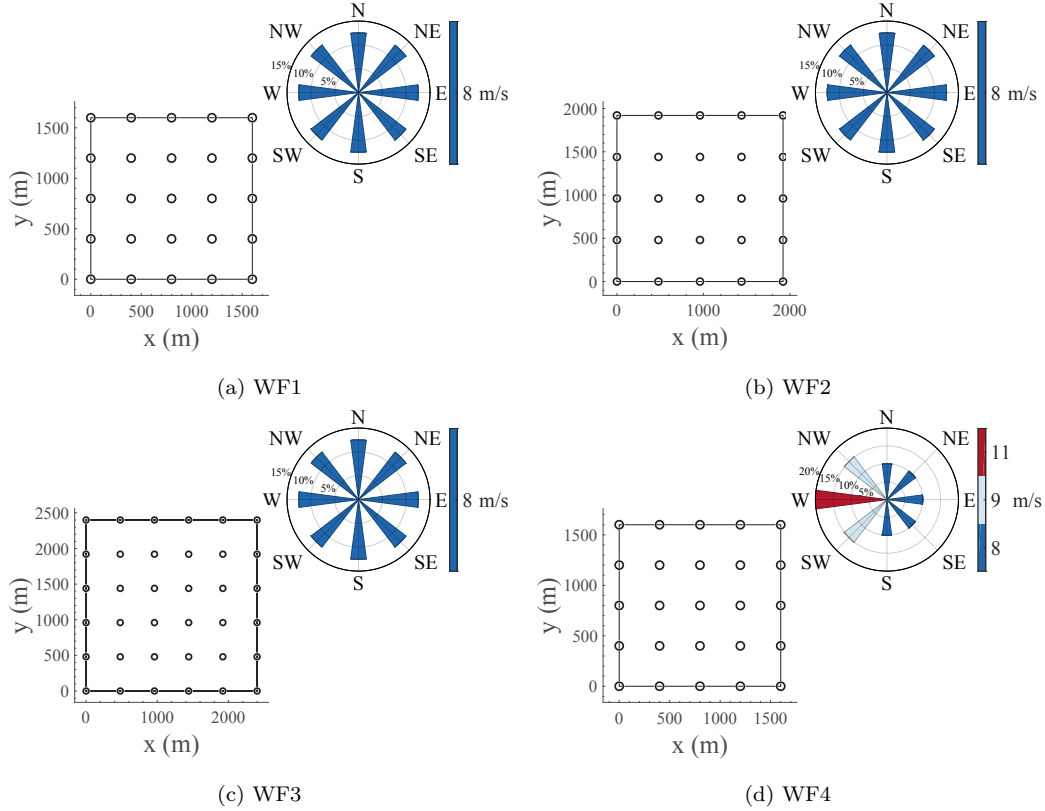


Figure 6: Four different optimization cases. (a) Optimization of a layout of 25 Vestas V80 wind turbines considering a uniform wind of 8 m/s in a square-shaped wind farm with a side length of 1600 m. The side length is $4 \times 5D$ where D is the wind turbine diameter (80 m). (b) Optimization of a layout of 25 Vestas V80 wind turbines considering a uniform wind of 8 m/s in a square-shaped wind farm with a side length of 1920 m. The side length is $4 \times 6D$. (c) Optimization of a layout of 36 Vestas V80 wind turbines considering a uniform wind of 8 m/s in a square-shaped wind farm with a side length of 2400 m. The side length is $5 \times 6D$. (d) Optimization of a layout of 25 Vestas V80 wind turbines considering uneven winds in a square-shaped wind farm with a side length of 1600 m. The side length is $4 \times 5D$.

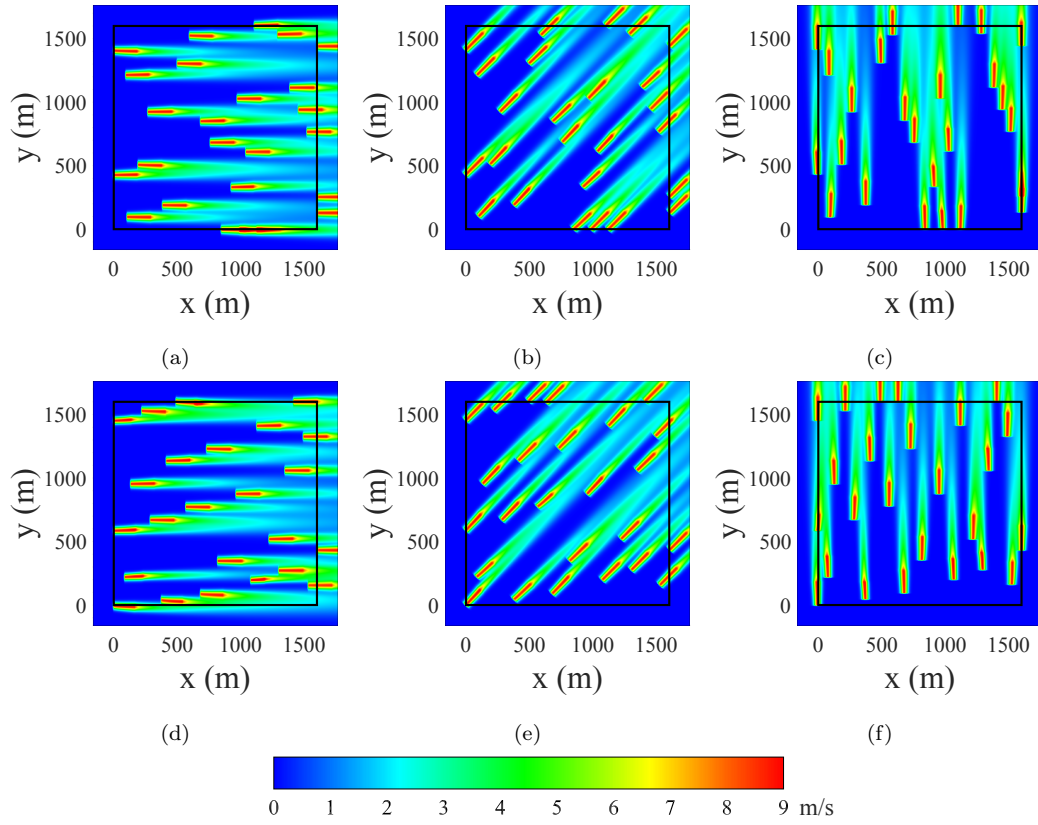


Figure 7: Contours of wakes of sequentially optimized layouts for the wind from (a) the west, (b) the southwest, and (c) the south. Contours of wakes of jointly optimized layouts for the wind from (a) the west, (b) the southwest, and (c) the south. The color bar corresponds the magnitude of the wake deficit.

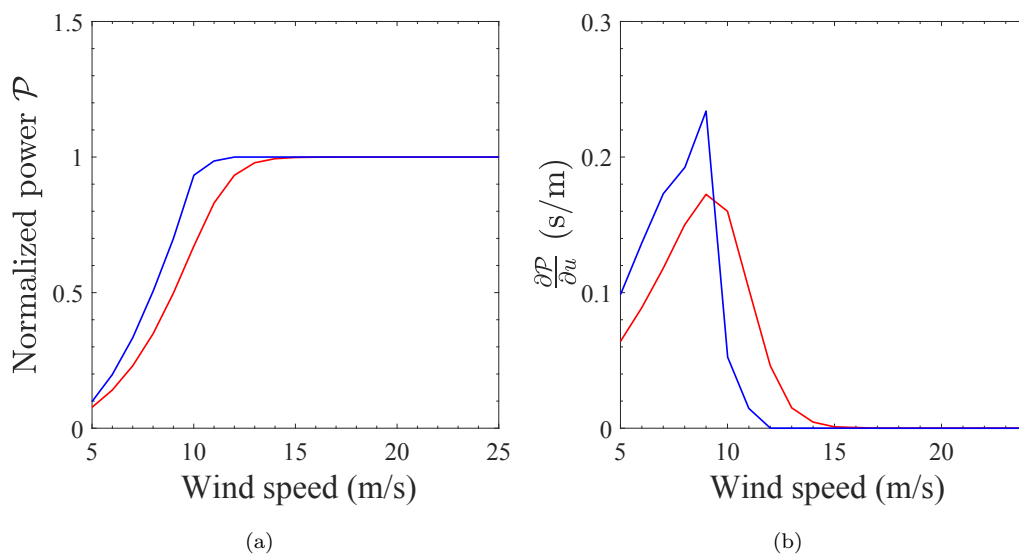


Figure 8: (a) Power curves of wind turbines normalized by the rated power and (b) derivatives of the power curve with respect to wind speed. Wind turbines are the Vestas V80 (—) and the Vestas V112 (—).